Determination of the Longitudinal Proton Structure Function $F_L(x, Q^2)$ at Low x

H1 Collaboration

Abstract:

A measurement of the inclusive cross section for the deep-inelastic scattering of positrons off protons at HERA is presented at momentum transfers $8.5 \leq Q^2 \leq 35$ GeV^2 and large inelasticity $y = 0.7$, i.e. for the Bjorken-x range $0.00013 \leq x \leq 0.00055$. Using a next-to-leading order QCD fit to the structure function F_2 at lower y values, the contribution of F_2 to the measured cross section at high y is calculated and, by subtraction, the longitudinal structure function F_L is determined for the first time with an average value of $F_L = 0.52 \pm 0.03$ (stat) $^{+0.25}_{-0.22}$ (syst) at $Q^2 = 15.4$ GeV^2 and $x = 0.000243$.

C. Adloff[35], S. Aid[13], M. Anderson[23], V. Andreev[26], B. Andrieu[29], C. Arndt[11], A. Babaev[25],
J. Bähr[36], J. Bán[18], Y. Ban[28], P. Baranov[26], E. Barrelet[30], R. Barschke[11], W. Bartel[11],
M. Barth[4], U. Bassler[30], H.P. Beck[38], M. Beck[14], H.-J. Behrend[11], A. Belousov[26], Ch. Berger[1],
G. Bernardi[30], G. Bertrand-Coremans[4], M. Besançon[9], R. Beyer[11], P. Biddulph[23],
P. Bispham[23], J.C. Bizot[28], V. Blobel[13], J. Blümlein[36], K. Borras[8], F. Botterweck[27],
V. Boudry[29], A. Braemer[15], W. Braunschweig[1], V. Brisson[28], W. Brückner[14], P. Bruel[29],
D. Bruncko[18], C. Brune[16], R. Buchholz[11], L. Büngener[13], J. Bürger[11], F.W. Büsser[13],
A. Buniatian[4], S. Burke[19], M.J. Burton[23], D. Calvet[24], A.J. Campbell[11], T. Carli[27],
M. Charlet[11], D. Clarke[5], A.B. Clegg[19], B. Clerbaux[4], S. Cocks[20], J.G. Contreras[8],
C. Cormack[20], J.A. Coughlan[5], A. Courau[28], M.-C. Cousinou[24], G. Cozzika[9], L. Criegee[11],
D.G. Cussans[5], J. Cvach[31], S. Dagoret[30], J.B. Dainton[20], W.D. Dau[17], K. Daum[42], M. David[9],
C.L. Davis[19,39], B. Delcourt[28], A. De Roeck[11], E.A. De Wolf[4], M. Dirkmann[8], P. Dixon[19],
P. Di Nezza[33], W. Dlugosz[7], C. Dollfus[38], K.T. Donovan[21], J.D. Dowell[3], H.B. Dreis[2],
A. Droutskoi[25], O. Dünger[13], H. Duhm[12,†] J. Ebert[35], T.R. Ebert[20], G. Eckerlin[11],
V. Efremenko[25], S. Egli[38], R. Eichler[37], F. Eisele[15], E. Eisenhandler[21], E. Elsen[11],
M. Erdmann[15], W. Erdmann[37], A.B. Fahr[13], L. Favart[28], A. Fedotov[25], R. Felst[11], J. Feltesse[9],
J. Ferencei[18], F. Ferrarotto[33], K. Flamm[11], M. Fleischer[8], M. Flieser[27], G. Flügge[2],
A. Fomenko[26], J. Formánek[32], J.M. Foster[23], G. Franke[11], E. Fretwurst[12], E. Gabathuler[20],
K. Gabathuler[34], F. Gaede[27], J. Garvey[3], J. Gayler[11], M. Gebauer[36], H. Genzel[1],
R. Gerhards[11], A. Glazov[36], L. Goerlich[6], N. Gogitidze[26], M. Goldberg[30], D. Goldner[8],
K. Golec-Biernat[6], B. Gonzalez-Pineiro[30], I. Gorelov[25], C. Grab[37], H. Grässler[2],
T. Greenshaw[20], R.K. Griffiths[21], G. Grindhammer[27], A. Gruber[27], C. Gruber[17], T. Hadig[1],
D. Haidt[11], L. Hajduk[6], T. Haller[14], M. Hampel[1], W.J. Haynes[5], B. Heinemann[13],
G. Heinzelmann[13], R.C.W. Henderson[19], H. Henschel[36], I. Herynek[31], M.F. Hess[27],
K. Hewitt[3], W. Hildesheim[11], K.H. Hiller[36], C.D. Hilton[23], J. Hladký[31], M. Höppner[8],
D. Hoffmann[11], T. Holtom[20], R. Horisberger[34], V.L. Hudgson[3], M. Hütte[8], M. Ibbotson[23],
Ç. İşsever[8], H. Itterbeck[1], A. Jacholkowska[28], C. Jacobsson[22], M. Jaffre[28], J. Janoth[16],
D.M. Jansen[14], T. Jansen[11], L. Jönsson[22], D.P. Johnson[4], H. Jung[22], P.I.P. Kalmus[21],
M. Kander[11], D. Kant[21], R. Kaschowitz[2], U. Kathage[17], J. Katzy[15], H.H. Kaufmann[36],
O. Kaufmann[15], M. Kausch[11], S. Kazarian[11], I.R. Kenyon[3], S. Kermiche[24], C. Keuker[1],
C. Kiesling[27], M. Klein[36], C. Kleinwort[11], G. Knies[11], T. Köhler[1], J.H. Köhne[27],
H. Kolanoski[36,41], S.D. Kolya[23], V. Korbel[11], P. Kostka[36], S.K. Kotelnikov[26],
T. Krämerkämper[8], H. Krehbiel[11], D. Krücker[27], H. Küster[22], M. Kuhlen[27], T. Kurča[36],
J. Kurzhöfer[8], D. Lacour[30], B. Laforge[9], M.P.J. Landon[21], W. Lange[36], U. Langenegger[37],
A. Lebedev[26], F. Lehner[11], S. Levonian[29], G. Lindström[12], M. Lindstroem[22], F. Linsel[11],
J. Lipinski[13], B. List[11], G. Lobo[28], P. Loch[11,43], J.W. Lomas[23], G.C. Lopez[12], V. Lubimov[25],
D. Lüke[8,11], L. Lytkin[14], N. Magnussen[35], E. Malinovski[26], R. Maracek[18], P. Marage[4],
J. Marks[24], R. Marshall[23], J. Martens[35], G. Martin[13], R. Martin[20], H.-U. Martyn[1],
J. Martyniak[6], T. Mavroidis[21], S.J. Maxfield[20], S.J. McMahon[20], A. Mehta[5], K. Meier[16],
F. Metlica[14], A. Meyer[13], A. Meyer[11], H. Meyer[35], J. Meyer[11], P.-O. Meyer[2], A. Migliori[29],
S. Mikocki[6], D. Milstead[20], J. Moeck[27], F. Moreau[29], J.V. Morris[5], E. Mroczko[6], D. Müller[38],
G. Müller[11], K. Müller[11], P. Murín[18], V. Nagovizin[25], R. Nahnhauer[36], B. Naroska[13],
Th. Naumann[36], I. Négri[24], P.R. Newman[3], D. Newton[19], H.K. Nguyen[30], T.C. Nicholls[3],
F. Niebergall[13], C. Niebuhr[11], Ch. Niedzballa[1], H. Niggli[37], G. Nowak[6], G.W. Noyes[5],
T. Nunnemann[14], M. Nyberg-Werther[22], M. Oakden[20], H. Oberlack[27], J.E. Olsson[11],
D. Ozerov[25], P. Palmen[2], E. Panaro[11], A. Panitch[4], C. Pascaud[28], G.D. Patel[20], H. Pawletta[2],
E. Peppel[36], E. Perez[9], J.P. Phillips[20], A. Pieuchot[24], D. Pitzl[37], G. Pope[7], B. Povh[14],

S. Prell[11], K. Rabbertz[1], G. Rädel[11], P. Reimer[31], S. Reinshagen[11], S. Riemersma[36], H. Rick[8],
F. Riepenhausen[2], S. Riess[13], E. Rizvi[21], P. Robmann[38], H.E. Roloff[36,†], R. Roosen[4],
K. Rosenbauer[1], A. Rostovtsev[25], F. Rouse[7], C. Royon[9], K. Rüter[27], S. Rusakov[26],
K. Rybicki[6], D.P.C. Sankey[5], P. Schacht[27], S. Schiek[13], S. Schleif[16], P. Schleper[15],
W. von Schlippe[21], D. Schmidt[35], G. Schmidt[13], L. Schoeffel[9], A. Schöning[11], V. Schröder[11],
E. Schuhmann[27], B. Schwab[15], F. Sefkow[38], R. Sell[11], A. Semenov[25], V. Shekelyan[11],
I. Sheviakov[26], L.N. Shtarkov[26], G. Siegmon[17], U. Siewert[17], Y. Sirois[29], I.O. Skillicorn[10],
P. Smirnov[26], V. Solochenko[25], Y. Soloviev[26], A. Specka[29], J. Spiekermann[8], S. Spielman[29],
H. Spitzer[13], F. Squinabol[28], P. Steffen[11], R. Steinberg[2], H. Steiner[11,40], J. Steinhart[13],
B. Stella[33], A. Stellberger[16], J. Stier[11], J. Stiewe[16], U. Stößlein[36], K. Stolze[36], U. Straumann[15],
W. Struczinski[2], J.P. Sutton[3], S. Tapprogge[16], M. Taševský[32], V. Tchernyshov[25],
S. Tchetchelnitski[25], J. Theissen[2], C. Thiebaux[29], G. Thompson[21], N. Tobien[11],
R. Todenhagen[14], P. Truöl[38], G. Tsipolitis[37], J. Turnau[6], J. Tutas[15], E. Tzamariudaki[11],
P. Uelkes[2], A. Usik[26], S. Valkár[32], A. Valkárová[32], C. Vallée[24], D. Vandenplas[29], P. Van Esch[4],
P. Van Mechelen[4], Y. Vazdik[26], P. Verrecchia[9], G. Villet[9], K. Wacker[8], A. Wagener[2],
M. Wagener[34], B. Waugh[23], G. Weber[13], M. Weber[16], D. Wegener[8], A. Wegner[27],
T. Wengler[15], M. Werner[15], L.R. West[3], T. Wilksen[11], S. Willard[7], M. Winde[36],
G.-G. Winter[11], C. Wittek[13], M. Wobisch[2], E. Wünsch[11], J. Žáček[32], D. Zarbock[12],
Z. Zhang[28], A. Zhokin[25], P. Zini[30], F. Zomer[28], J. Zsembery[9], K. Zuber[16], and M. zurNedden[38]

[1] *I. Physikalisches Institut der RWTH, Aachen, Germany[a]*
[2] *III. Physikalisches Institut der RWTH, Aachen, Germany[a]*
[3] *School of Physics and Space Research, University of Birmingham, Birmingham, UK[b]*
[4] *Inter-University Institute for High Energies ULB-VUB, Brussels; Universitaire Instelling Antwerpen, Wilrijk; Belgium[c]*
[5] *Rutherford Appleton Laboratory, Chilton, Didcot, UK[b]*
[6] *Institute for Nuclear Physics, Cracow, Poland[d]*
[7] *Physics Department and IIRPA, University of California, Davis, California, USA[e]*
[8] *Institut für Physik, Universität Dortmund, Dortmund, Germany[a]*
[9] *CEA, DSM/DAPNIA, CE-Saclay, Gif-sur-Yvette, France*
[10] *Department of Physics and Astronomy, University of Glasgow, Glasgow, UK[b]*
[11] *DESY, Hamburg, Germany[a]*
[12] *I. Institut für Experimentalphysik, Universität Hamburg, Hamburg, Germany[a]*
[13] *II. Institut für Experimentalphysik, Universität Hamburg, Hamburg, Germany[a]*
[14] *Max-Planck-Institut für Kernphysik, Heidelberg, Germany[a]*
[15] *Physikalisches Institut, Universität Heidelberg, Heidelberg, Germany[a]*
[16] *Institut für Hochenergiephysik, Universität Heidelberg, Heidelberg, Germany[a]*
[17] *Institut für Reine und Angewandte Kernphysik, Universität Kiel, Kiel, Germany[a]*
[18] *Institute of Experimental Physics, Slovak Academy of Sciences, Košice, Slovak Republic[f,j]*
[19] *School of Physics and Chemistry, University of Lancaster, Lancaster, UK[b]*
[20] *Department of Physics, University of Liverpool, Liverpool, UK[b]*
[21] *Queen Mary and Westfield College, London, UK[b]*
[22] *Physics Department, University of Lund, Lund, Sweden[g]*
[23] *Physics Department, University of Manchester, Manchester, UK[b]*
[24] *CPPM, Université d'Aix-Marseille II, IN2P3-CNRS, Marseille, France*
[25] *Institute for Theoretical and Experimental Physics, Moscow, Russia*
[26] *Lebedev Physical Institute, Moscow, Russia[f]*

[27] *Max-Planck-Institut für Physik, München, Germany*[a]

[28] *LAL, Université de Paris-Sud, IN2P3-CNRS, Orsay, France*

[29] *LPNHE, Ecole Polytechnique, IN2P3-CNRS, Palaiseau, France*

[30] *LPNHE, Universités Paris VI and VII, IN2P3-CNRS, Paris, France*

[31] *Institute of Physics, Czech Academy of Sciences, Praha, Czech Republic*[f,h]

[32] *Nuclear Center, Charles University, Praha, Czech Republic*[f,h]

[33] *INFN Roma 1 and Dipartimento di Fisica, Università Roma 3, Roma, Italy*

[34] *Paul Scherrer Institut, Villigen, Switzerland*

[35] *Fachbereich Physik, Bergische Universität Gesamthochschule Wuppertal, Wuppertal, Germany*[a]

[36] *DESY, Institut für Hochenergiephysik, Zeuthen, Germany*[a]

[37] *Institut für Teilchenphysik, ETH, Zürich, Switzerland*[i]

[38] *Physik-Institut der Universität Zürich, Zürich, Switzerland*[i]

[39] *Visitor from Physicss Dept. University Louisville, USA*

[40] *On leave from LBL, Berkeley, USA*

[41] *Institut für Physik, Humboldt-Universität, Berlin, Germany*[a]

[42] *Rechenzentrum, Bergische Universität Gesamthochschule Wuppertal, Wuppertal, Germany*[a]

[43] *Physics Department, University of Arizona, Tuscon, USA*

[†] *Deceased*

1   Introduction

Precise measurements of the inclusive scattering cross section at the ep collider HERA are important for the understanding of proton substructure. In the one-photon exchange approximation, which is valid in the kinematic domain explored here, the deep inelastic scattering (DIS) cross section is given by the expression

$$\frac{d^2\sigma}{dxdQ^2} = \frac{2\pi\alpha^2}{Q^4 x} \cdot [(2(1-y)+y^2)F_2(x,Q^2) - y^2 F_L(x,Q^2)]. \tag{1}$$

Here Q^2 is the squared four-momentum transfer, x denotes the Bjorken scaling variable, $y = Q^2/sx$ is the inelasticity, with s the ep center of mass energy squared, and α is the fine structure constant. The structure functions F_2 and F_L are related to the cross sections σ_T and σ_L for the interaction of transversely and longitudinally polarized virtual photons with protons. In the Quark Parton Model F_2 is the sum of quark and antiquark distributions multiplied by x and weighted with the square of the electric charges of the quarks, while F_L is predicted to be zero for spin 1/2 partons [1]. In Quantum Chromodynamics (QCD) F_L acquires a non zero value due to gluon radiation which is proportional to the strong coupling constant α_s [2] with possibly sizeable higher order corrections in QCD perturbation theory [3]. Measurements of F_L, expressed as the structure function ratio

$$R = \frac{F_L}{F_2 - F_L} = \frac{\sigma_L}{\sigma_T}, \tag{2}$$

have been made by various fixed target lepton-hadron scattering experiments at higher x values [4, 5]. This paper presents the first determination of $F_L(x,Q^2)$ at HERA in the deep inelastic region of $8.5 \le Q^2 \le 35$ GeV^2 and very small x values between $1.3 \cdot 10^{-4}$ and $5.5 \cdot 10^{-4}$.

The H1 collaboration has recently reported a measurement of the structure function F_2 [6] in the range $3 \cdot 10^{-5} \le x \le 0.32$ and $1.5 \le Q^2 \le 5000$ GeV^2, using data taken in the year 1994. The measurement was restricted to y values between 0.01 and 0.6 where the contribution of F_2 to the cross section, Eq. (1), dominates. The F_2 values were extracted from the measured cross sections assuming theoretically computed values of F_L. A next-to-leading order (NLO) QCD analysis showed that the F_2 structure function can be well described by the DGLAP evolution equations [7] in the kinematic range of the measurement.

At high y the factors $Y_+ = 2(1-y)+y^2$ and y^2 multiplying F_2 and F_L, respectively, are of comparable size. Therefore, the usual technique of extracting F_2 assuming a calculated F_L is reversed and F_L is determined by subtraction of the F_2 contribution from the measured cross section. The following procedure is applied. Our measurement of F_2 [6], for $y < 0.35$, and fixed target data at larger x [8] are used to extract the parton distribution functions which are evolved in Q^2 according to the NLO DGLAP evolution equations. This provides predictions for the structure function F_2 in the high y region which allow, by subtraction of the contribution of F_2 to the DIS cross section (cf. Eq. (1)), the determination of the longitudinal structure function F_L to be made. Note that the measurements of F_2 are well described by NLO QCD over four orders of magnitude in x and Q^2 while the evolution required here extends the maximum Q^2 at fixed x by a factor of two only. Nevertheless, since an extended kinematic region is accessed here, where new effects could be important, it can not be excluded that the structure function F_2 behaves differently than assumed.

Instead of subtracting the contribution of F_2 from the cross section one could perform a cross section analysis using the QCD predictions for both structure functions F_2 and F_L. This would

be conceptually different to the method employed in this paper because then an assumption would be required not only for F_2 but also for F_L which is less well known than F_2.

A salient feature of the subtraction method is a partial cancelation of systematic errors because the cross sections at low and at high y are measured using one common set of data. The experimental challenge is to measure the cross section at high y where the energy of the scattered positron E'_e is comparatively low. The present measurement is made for $11 \geq E'_e \geq 6.5$ GeV, or $0.6 < y < 0.78$, which is an extension of the kinematic range covered by our previously published measurement of F_2 [6]. An understanding of the trigger efficiency, positron identification, photoproduction background and radiative corrections now becomes more demanding.

The paper is organized as follows. Section 2 discusses the cross section measurement with particular emphasis on the high y region. Section 3 describes the QCD fit used to define the F_2 contribution for subtraction and presents the final results. A short summary is given in Section 4.

2   Cross Section Measurement

2.1   Kinematics

In 1994 HERA was operated with positrons of energy $E_e = 27.5$ GeV and protons of energy $E_p = 820$ GeV. The event kinematics were reconstructed using the energy of the scattered positron E'_e and the polar angle θ_e according to the relations

$$Q^2_e = \frac{E'^2_e \sin^2 \theta_e}{1 - y_e} \qquad\qquad y_e = 1 - \frac{E'_e}{E_e} \sin^2(\theta_e/2). \qquad\qquad (3)$$

Here θ_e is defined with respect to the proton beam direction, defining the z axis, and x is calculated as Q^2/sy with $s = 4E_eE_p$. At high y the determination of Q^2 and y from the reconstructed positron, rather than from the final state hadrons or a combination of both, is preferred because of the superior resolutions in Q^2 and x. The determination of the inclusive event kinematics using the variables E'_e and θ_e is subsequently referred to as the "electron method".

The previously published analysis [6] used the "sigma method" to determine $F_2(x, Q^2)$ for $y < 0.15$. This method combines the positron with the hadronic measurement by defining

$$Q^2_\Sigma = \frac{E'^2_e \sin^2 \theta_e}{1 - y_\Sigma} \qquad\qquad y_\Sigma = \frac{y_h}{1 + y_h - y_e}, \qquad\qquad (4)$$

which avoids the resolution degradation of y_e at low y. Here

$$y_h = \frac{\sum_i (E_i - p_{z,i})}{2E_e}, \qquad\qquad (5)$$

where E_i and $p_{z,i}$ are the energy and longitudinal momentum component of a particle i. The summation extends over all hadronic final state particles and the masses are neglected.

The kinematic region of the F_L measurement was limited by the constraints $0.6 < y < 0.78$, $155^o < \theta_e < 171^o$. It was divided into six intervals of Q^2 with the limits (7.5, 10.0, 13.3, 17.8, 23.7, 31.6, 42.2) GeV^2 and with central values chosen to be (8.5, 12.0, 15.0, 20.0, 25.0, 35.0) GeV^2 or the corresponding values of $x = Q^2/sy$ at $y = 0.7$.

2.2   The H1 Detector

The H1 detector [9] is a nearly hermetic apparatus built to investigate high-energy ep interactions at HERA. The measurement of the inclusive deep inelastic cross section relies essentially on the inner tracking chamber system and on the backward electromagnetic and liquid argon calorimeters. A superconducting solenoid surrounds both the tracking system and the liquid argon calorimeter, providing a uniform magnetic field of 1.15 T.

The energy of the scattered positron was measured in the backward electromagnetic calorimeter (BEMC) behind which a scintillator hodoscope (TOF) was placed to veto proton beam induced background interactions. The identification of the scattered positron and the measurement of the polar angle made use of the backward multiwire proportional chamber (BPC) which was attached to the BEMC. In the kinematic range of this F_L measurement the positron angle was limited to $155° < \theta_e < 171°$. For these angles the scattered positron traversed the inner cylindrical proportional chamber (CIP) which could therefore be included in the positron identification requirement. The inner and outer proportional chambers (CIP at 18 cm radius and COP at 47 cm radius) were used in the trigger to reconstruct tracks of particles originating from the interaction region, and thus to reduce beam induced background events. The interaction vertex was determined with the central drift chambers and the hadronic final state was reconstructed with the Liquid Argon calorimeter and the tracking detectors.

The luminosity was determined from the cross section of the elastic bremsstrahlung process, $ep \to ep\gamma$, measured with a precision of 1.5%. The integrated luminosity for this analysis is 1.25 pb^{-1}. The final state positron and the photon scattered at very low Q^2 can be detected in calorimeters ("electron and photon taggers") which are situated 33 m and 103 m from the interaction point in the positron beam direction.

The use of the H1 detector for the inclusive DIS cross section measurement is further discussed in [6]. A detailed technical description of the apparatus can be found in [9].

2.3   Trigger

The DIS event selection was based on events triggered in the BEMC by an energy deposition of more than 6 GeV, combined with a TOF requirement and a valid CIP-COP track signal. The efficiency of the BEMC energy requirement was monitored using a central track trigger and found to be better than 99% for the whole analysis region. The CIP-COP trigger required at least one track pointing to the interaction region. The efficiency was 96% after all selection cuts. It was found to vary little over the region of acceptance and to be well reproduced by the simulation of the trigger response. It was monitored down to a positron energy of 7.5 GeV by an independent BEMC trigger and was evaluated between 6.5 and 7.5 GeV by studying its dependence on θ_e, on the hadronic angle and on the charged track multiplicity comparing simulation with data.

2.4   Event Selection

The event selection criteria are summarized in Table 1. The positron was identified as the most energetic cluster in the BEMC associated with a signal in the preceding BPC and, if geometrically accessible, in the CIP. For the determination of the event kinematics and background suppression a vertex had to be reconstructed with more than one track in the central drift chamber.

6

6.5 GeV$< E_e' <$ 11 GeV
$\epsilon_1 < 4$ cm
$\epsilon_2 < 3.5$ cm
$\epsilon_3 < 5$ cm
-25 cm$< z_{vtx} < 35$ cm
$N_{tr} > 1$

Table 1: *Summary of event selection criteria. For positron identification three estimators were used - ϵ_1: reconstructed positron cluster radius in the BEMC; ϵ_2: distance from the closest BPC hit to the centroid of the positron cluster; ϵ_3: distance from the positron candidate trajectory to the closest active CIP pad (not used for tracks outside the CIP acceptance region). z_{vtx} denotes the z position of the reconstructed interaction vertex and N_{tr} is the number of charged tracks reconstructed in the central drift chambers.*

Deep inelastic events were generated using the DJANGO [10] program which is based on HERACLES [11] for the electroweak interaction and on LEPTO [12] to simulate the hadronic final state. Photoproduction background was generated with the PHOJET [13] program. The detector response was simulated using a program based on GEANT [14]. The simulated events were subjected to the same reconstruction and analysis chain as the data. For comparisons with experimental distributions, all simulated spectra were normalized to the measured luminosity.

Fig. 1a shows the distribution of the energy of the scattered positron for the events passing all selection criteria in the high y region. The experimental distribution is very well described by the superposition of the simulated spectra from DIS events and of the photoproduction background, discussed below.

For the genuine DIS events at high y, the current jet particles are on average emitted backwards with respect to the proton beam direction. Thus there is a possibility that the largest energy cluster is not due to the scattered positron but to a hadronic energy deposition in the BEMC. In a Monte Carlo simulation of DIS events 3% of the selected positron candidates were found to be produced by the hadronic final state. In more than 99% of the simulated events the genuine positron was either the highest energy or second highest energy cluster. For a comparative study of the effect of misidentification at low energies, a positron finding algorithm was used which accepted an event even if the highest energy cluster failed to satisfy the selection conditions but the second highest energy cluster fulfilled them. The resulting cross section agreed to within 1% with that based on the standard positron finding algorithm which used the highest energy cluster. Fig. 1b shows the BEMC energy distribution of the cluster with second highest energy which is well reproduced by the simulation. The background due to photoproduction is small because there is only a small probability to generate two high energy clusters in the BEMC in such events.

2.5 Photoproduction Background

At low energies and for large polar angles of the scattered positron there are two major sources of background in the candidate DIS events. Non-ep background occurs due to beam interactions with residual gas and beam-line elements. An effective filter against such events is the requirement of a reconstructed event vertex in the interaction region. The number of remaining beam-induced background events was estimated to be 2.5% in the lowest Q^2 interval and below 1% everywhere else using non-colliding bunch events.

The second, more difficult, background source is photoproduction, including low Q^2 DIS

events, in which the scattered positron escapes undetected along the beam pipe and in which an energy cluster from the final state particles fakes a positron signal in the BEMC. The typical characteristic of the γp background is a rapid rise of the cross section towards lower cluster energy. Most frequently, the energy cluster in the BEMC is produced by a π^0 decay to two photons or by charged hadrons, mainly $\pi^{\pm}$. Energy clusters due to neutral particles are effectively removed by demanding a track pattern in the CIP and the requirement that a BPC hit coincide spatially with a BEMC cluster. Hadronic clusters typically have large cluster radii in the BEMC, and are rejected by the cut on ϵ_1, see Table 1.

The Monte Carlo simulation was used to subtract bin by bin the remaining photoproduction background. A fraction of photoproduction interactions had the genuine final state positron detected ("tagged") in the electron tagger. Fig. 2a shows the BEMC energy cluster distribution for such events which passed the selection criteria. Within the accepted range in energy (6.5 to 11 GeV) the simulation reproduces the observed rate to within 4%.

A further study was based on events with large energy cluster radius (ϵ_1) or without CIP validation (ϵ_3). These samples predominantly consist of photoproduction events. The event sample rejected by the ϵ_1 cut (Table 1) allows the study of faked positron signals by charged hadrons. The shape of the energy spectrum agrees well with the simulated distribution and the normalization is reproduced to within 7%. The event sample rejected by the ϵ_3 cut allows the study of π^0 induced background. The fake positron energy distribution of events in this sample is shown in Fig. 2b. The normalization agrees to within 2% of the simulated rate.

The photoproduction background amounts to $< 20\%$ for the lowest Q^2 interval and decreases to $< 5\%$ for the highest Q^2 interval. The normalization uncertainty was estimated to be 20% taking into account the fluctuations per bin of the simulated sample and also the fact that only part of the photoproduction events, with positron energies between 5 GeV and 15 GeV, is tagged.

2.6 Cross Section Determination

The deep inelastic scattering cross section was obtained by correcting the background subtracted number of events with the acceptance calculated from the Monte Carlo events, normalized to the measured luminosity. The cross section was corrected for higher order QED and electroweak contributions using the HECTOR [15] program. Starting from the GRV [16] parton distributions, a two step iterative analysis was performed to calculate the acceptance and the radiative corrections. This maintains the uncertainty of the cross section measurement due to input structure function variations below 1%.

The radiative corrections were calculated to order α^2 with soft photon exponentiation [15, 17]. Taking into account the hadronic track requirements they are about 35%. Detailed comparisons were made between the HECTOR result and the HERACLES [11] Monte Carlo simulation which showed agreement at the per cent level. A study has also been made comparing the cross section results with and without a selection $y_h > 0.1$ which, when applied, reduces the radiative corrections to about 15%. The resulting cross sections agreed to within 2%.

The systematic error on the cross section is derived from the following contributions:

- A 1% uncertainty of the BEMC energy scale [18] leads to an error of about 1.5%.

- A 1 mrad uncertainty of the measured polar angle of the positron causes a 2% error.

- The radiative corrections lead to a cross section uncertainty of 2%.

- The vertex reconstruction efficiency is known to 2% apart from the lowest Q^2 interval where a 4% error was estimated.

- As in [6] an efficiency error of 2% is assigned to account for global event selection, BPC efficiency and TOF veto uncertainties.

- The various cut efficiencies, studied using different deep inelastic and background enriched data and simulated samples, lead to an estimated systematic error of 3% including the trigger efficiency error.

- An extra error of 1% is estimated for positron misidentification effects using the Monte Carlo simulation and the study of the stability of the measurement against ignoring or considering the second highest energy cluster in the BEMC.

- The photoproduction background was known to within 20%. This leads to a 4% error at $Q^2 = 8.5$ GeV^2 decreasing to 1% at $Q^2 = 35$ GeV^2.

Statistical errors in the Monte Carlo acceptance and efficiency calculations were computed and added quadratically to the systematic error. The total systematic error on the cross section is about 8% at $Q^2 = 8.5$ GeV^2 and about 6% for the higher Q^2 values. Most of the error sources scale with E'_e and are only weakly dependent on θ_e in the range of the F_L determination. The statistical error is about three times smaller than the systematic error.

Q^2/GeV^2	x	$\kappa\sigma$	Δ_{stat}	Δ_{syst}	F_2	Δ_{stat}	Δ_{syst}	R_{calc}
8.5	0.000135	1.165	0.027	0.095	1.354	0.031	0.110	0.45
12.0	0.000190	1.198	0.026	0.075	1.375	0.030	0.086	0.40
15.0	0.000238	1.368	0.032	0.079	1.561	0.037	0.090	0.38
20.0	0.000317	1.276	0.034	0.071	1.445	0.038	0.080	0.35
25.0	0.000396	1.439	0.042	0.079	1.651	0.048	0.091	0.39
35.0	0.000554	1.435	0.062	0.077	1.634	0.071	0.088	0.37

Table 2: *Inclusive cross section $\sigma = d^2\sigma/dxdQ^2$, eq.(1), scaled by the kinematic factor $\kappa = Q^4x/(2\pi\alpha^2 \cdot Y_+)$ with statistical and systematic errors. The Q^2, x values correspond to $y = 0.7$ in all bins. Also quoted are the values of F_2 corresponding to these cross section measurements with calculated R values, given in the rightmost column. The values of $R = R_{calc}$ were obtained using the GRV parton distributions [16] as input. There is an additional, overall normalization uncertainty of 1.5% due to the luminosity measurement error.*

The ep cross section is given in Table 2 for the six new intervals in Q^2 and x. The analysis was also extended into the region of our previously published F_2 results for $0.6 > y > 0.03$. In Fig. 3 the present cross section measurement is shown together with the data [6]. There is everywhere good agreement in the region of overlap. The cross section is quoted in the form $\sigma \cdot Q^4x/(2\pi\alpha^2 \cdot Y_+) = F_2 - y^2F_L/Y_+$ which for small y is about equal to F_2 independently of F_L. The three lines drawn in Fig. 3 represent cross sections calculated using the QCD fit for F_2 which is described in the subsequent section and three different assumptions on F_L. The dashed-dotted and dashed lines correspond to the limits $F_L = 0$ and $F_L = F_2$, respectively, as required by the positivity of the cross sections σ_L and σ_T. The solid line represents the cross section with F_L calculated using the gluon and quark distributions obtained by the QCD

9

analysis of F_2. It becomes apparent in Fig. 3 that at lowest x, corresponding to the high y region of this data, the cross section becomes very sensitive to the longitudinal structure function. On the contrary, at larger x, for about $y < 0.35$, the F_2 contribution dominates and the three lines nearly coincide. Most of the previously published F_2 data points are insensitive to the assumptions on F_L.

In the publication [6] the measured DIS cross section was used to determine the structure function F_2 assuming R to be given by the GRV parton distributions [16] using the relation [19]. This measurement represents an extension of the previous cross section data towards lower x. In order to provide a consistent set of structure function values the corresponding six values of F_2 were derived following the same procedure (see Table 2). Note that these values are rather sensitive to the R values chosen.

3 Determination of F_L

3.1 QCD Fit

For the subtraction of the F_2 contribution to the cross section a NLO QCD fit was performed using the DGLAP evolution equations. The fit used the H1 data [6] for $y < 0.35$. The BCDMS proton and deuterium data [8] were used to constrain the high x behaviour of the parton distributions. In contrast with the previous QCD analysis performed by H1 [6], the NMC data [20] were not included in the standard fit to ensure a maximum weight of the H1 data in the fit procedure. The starting point of the evolution was chosen to be $Q_0^2 = 5$ GeV^2 and all data with $Q^2 \geq Q_{min}^2 = 1.5$ GeV^2 were included in the fit. To avoid possible higher twist effects, BCDMS data in the range $x > 0.5$ for $Q^2 < 15$ GeV^2 were not included in the fit. The normalization of the H1 data was kept fixed. The fit used three light flavors with the charm contribution added using the NLO calculation of the photon-gluon fusion process [16, 21]. Furthermore, the momentum sum rule was imposed and the integral over the valence quark distributions was set to 2 for u_v and to 1 for d_v. The input parton distributions at the starting scale Q_0^2 were parameterized as follows:

$$
\begin{aligned}
xg(x) &= A_g x^{B_g}(1-x)^{C_g}, \\
xu_v(x) &= A_u x^{B_u}(1-x)^{C_u}(1 + D_u x + E_u\sqrt{x}), \\
xd_v(x) &= A_d x^{B_d}(1-x)^{C_d}(1 + D_d x + E_d\sqrt{x}), \\
xS(x) &= A_S x^{B_S}(1-x)^{C_S}(1 + D_S x + E_S\sqrt{x}),
\end{aligned}
\tag{6}
$$

where $S = \bar{u} = \bar{d} = 2\bar{s}$ defines the sea distributions. Three fits with different, fixed Λ_{QCD} values were performed. The best χ^2/ndf of $506/(505\text{-}15)$ was obtained for $\Lambda_{QCD} = 210$ MeV. The fitted parton distribution functions were evolved into the new domain using the NLO DGLAP equations and used to calculate the corresponding values of F_2.

Table 3 summarizes the Q^2 averaged uncertainties in F_2 arising from the fit procedure. The total uncertainty due to the fit assumptions amounts to 1.7%. The resulting absolute error of the longitudinal structure function $\Delta F_L \simeq Y_+/y^2 \cdot \Delta F_2$ is approximately 0.07.

There is a small dependence of the structure function F_2 on F_L due to the assumption made for F_L in the cross section analysis for $y < 0.35$. Thus the two extreme assumptions $F_L = 0$ and $F_L = F_2$ were used and two modified structure functions F_2 were derived as input to two QCD fits. This changed the QCD predicted F_2 at $y = 0.7$ on average by -1.6% and $+3.8\%$,

fit assumption	uncertainty in %
NMC data used	1.4
change of Λ_{QCD} by 50 MeV	0.7
$g(x, Q_o^2) \cdot (1 + E\sqrt{x})$	0.1
$Q_{min}^2 = 5 \text{ GeV}^2$	0.6
$Q_o^2 = 3 \text{ GeV}^2$	0.4

Table 3: *Uncertainty, relative to the result of the standard fit (see text), of the structure function F_2 averaged over the Q^2 range of the F_L data for various assumptions in the QCD fit procedure.*

respectively. Thus an asymmetric error on F_L was introduced and was added in quadrature to the other systematic errors.

Two different cross checks were made of the prediction of F_2 at lowest x by using the perturbative dipole model with k_T factorization [22] and an empirical model based on the similarity of the rise of F_2 at low x and the evolution of the charged multiplicity with energy in e^+e^- collisions [23]. The model parameters were determined using the previously published H1 F_2 data [6] for $y < 0.35$ and Q^2 boundaries given by the limitations of these approaches. The three-parameter F_2 function in the dipole model, calculated at $y = 0.7$, is only 2% lower than the structure function obtained by the evolution procedure described above. Similarly, the two-parameter F_2 function of the empirical model is on average 2% higher than the QCD fit result at $y = 0.7$. Thus both approaches to extrapolate F_2 would lead to a result for the longitudinal structure function in very good agreement with the one obtained subsequently using the QCD fit for the description of F_2.

3.2 Results

The measured longitudinal structure function F_L is given in Table 4. The systematic error consists of the following contributions:

- The experimental errors of the cross section measurement which are uncorrelated with the error of the data entering the QCD fit at lower y. These are error sources, such as the tracking trigger or CIP efficiency, which are specific for the high y range and to this analysis.

- The error due to possible variations of the assumptions in the QCD fit procedure as discussed in Section 3.1.

- The experimental errors like energy and angle uncertainties and global efficiency and luminosity errors which are mostly common to both the low and the high y region. A correlation of these errors is introduced through the QCD fit of F_2. This error source includes also the statistical error of the fit result.

The third contribution comprises several effects. For example, any global shift common to the high y data and the H1 data used in the fit, like the luminosity uncertainty, gets reduced to about 1/3 of its magnitude. A reduction of the error is observed as well for the polar angle uncertainty. However, the error of the energy of the scattered positron is not compensated.

11

The H1 F_2 data [6] for $y \geq 0.15$ were obtained with the electron method and those at smaller y with the sigma method. A 1% increase in E'_e increases the cross section for $y \geq 0.15$ and decreases it below that value, a behaviour which leads to a large change in the χ^2 of the fit. Thus the measurement of the positron energy is the dominating "correlated" error although it has only a small effect on the cross section at high y.

Q^2/GeV^2	x	F_L	Δ_{stat}	$+\Delta_{syst}$	$-\Delta_{syst}$	Δ_{exp}^{unc}	Δ_{exp}^{cor}	Δ_{fit}
8.5	0.000135	0.51	0.06	0.29	0.27	0.17	0.19	0.06
12.0	0.000190	0.63	0.06	0.28	0.25	0.15	0.18	0.07
15.0	0.000238	0.35	0.08	0.29	0.27	0.15	0.19	0.08
20.0	0.000317	0.67	0.08	0.28	0.26	0.14	0.18	0.07
25.0	0.000396	0.33	0.10	0.25	0.22	0.15	0.14	0.07
35.0	0.000554	0.39	0.15	0.24	0.21	0.14	0.14	0.07

Table 4: *The longitudinal structure function F_L with statistical (Δ_{stat}) and systematic errors ($\pm\Delta_{syst}$): Δ_{exp}^{unc} is the uncorrelated experimental cross section error at high y, Δ_{exp}^{cor} is the correlated experimental error and Δ_{fit} is the error introduced by the QCD fit uncertainty. The total systematic error contains also the asymmetric contribution due to the assumptions on F_L in the determination of F_2, see Section 3.1. The Q^2, x values correspond to $y = 0.7$ in all bins.*

The six measurement values enable a determination to be made of the mean F_L and its derivative $dF_L/d\ln(x)$ for $Q^2 = 0.7 \cdot sx$ from a straight line $F_L = a + b \cdot \ln(x)$. Taking into account the error correlations between the six data points we obtain a mean $F_L = 0.52 \pm 0.03$ (stat) $^{+0.25}_{-0.22}$ (syst) and a derivative $dF_L/d\ln(x) = -0.085 \pm 0.080$ (stat) $^{+0.082}_{-0.083}$ (syst) at $Q^2 = 15.4$ GeV^2 and $x = 0.000243$. Note that the derivative has comparable statistical and systematic errors while the error of the mean F_L is dominated by systematics. Fig. 4 shows the data of Table 4 and the extreme limits of $F_L = 0$ and $F_L = F_2$ using the QCD fit. Without utilizing the measured dependence on x or Q^2, these extremes are excluded with 2.3 and 4.0 times the total error, respectively.

At low x the longitudinal structure function is related to the gluon distribution. The dashed band in Fig. 4 represents the calculation of F_L according to [3] for three light quarks and according to [21] for the charm contribution. The input gluon and quark distributions are determined by the NLO QCD fit described in Section 3.1. The width of this band is determined by the experimental errors of the F_2 data, taking into account their point-to-point correlations, and by the fit uncertainties discussed above. At the present level of accuracy there is consistency between the structure function F_L determined from this analysis and that calculated from the gluon and quark distributions.

4   Summary

Based on data taken in 1994 with a luminosity of 1.25 pb^{-1}, an inclusive measurement of the deep inelastic cross section measurement at $y = 0.7$ has been used to determine for the first time the longitudinal structure function $F_L(x, Q^2)$ at very low Bjorken x. The analysis assumed the proton structure function $F_2(x, Q^2)$ to be in accordance with next-to-leading order perturbative QCD. The result excludes the extreme limits of $F_L = 0$ and $F_L = F_2$, corresponding to $R = 0$ and $R = \infty$, by 2.3 and 4.0 times the total error on F_L. The result is consistent with a higher

order QCD calculation of F_L which essentially relied on the gluon distribution as determined from the F_2 structure function data.

Acknowledgments

References

[1] C.G. Callan and D. Gross, Phys. Rev. Lett. **22** (1969) 156.

[2] A. Zee, F. Wilczek and S.B. Treiman, Phys. Rev. **D 10** (1974) 2881.

[3] E.B. Zijlstra and W. van Neerven, Nucl. Phys. **B 383** (1992) 525;
S.A. Larin and J.A.M. Vermaseren, Z.Phys. **C 57** (1993) 93.

[4] L. Whitlow et al., Phys. Lett. **B 250** (1990) 193;
A.Bodek, Proceedings of the 4th International Conference on Deep Inelastic Scattering, Rome, April 1996, to be published, and references cited therein.

[5] NMC Collaboration, M. Arneodo et al., subm. to Nucl. Phys. **B**, hep-ph/9610231.

[6] H1 Collaboration, S. Aid et al., Nucl.Phys. **B 470** (1996) 3.

[7] Yu.L. Dokshitzer, Sov. Phys. JETP **46** (1977) 641;
V.N. Gribov and L.N. Lipatov, Sov. J. Nucl. Phys. **15** (1972) 438 and 675;
G. Altarelli and G. Parisi, Nucl. Phys. **B 126** (1977) 298.

[8] BCDMS Collaboration, A.C. Benvenuti et al., Phys. Lett. **B 223** (1989) 485;
CERN preprint CERN-EP/89-06 (1989).

[9] H1 Collaboration, S. Aid et al., DESY H1 note 96-01(1996), Nucl. Instr. and Meth. **A**, to appear.

[10] G.A. Schuler and H. Spiesberger, Proceedings of the Workshop Physics at HERA, DESY 1992, Eds. W. Buchmüller and G. Ingelman, vol.3, 1419.

[11] A. Kwiatkowski, H. Spiesberger and H.-J. Möhring, Comput. Phys. Comm. **69** (1992) 155.

[12] G. Ingelman, Proceedings of the Workshop Physics at HERA, vol. 3, Eds. W. Buchmüller and G. Ingelman, DESY (1992) 1366.

[13] R. Engel, Proceedings of the XXIXth Rencontres de Moriond, Ed. J. Tran Thanh Van (Editions Frontières, 1994) 321.

[14] R. Brun et al., GEANT3 User's Guide, CERN-DD/EE 84-1, Geneva (1987).

[15] A. Arbuzov et al., Comput. Phys. Comm. **94** (1996) 128.

[16] M. Glück, E. Reya and A. Vogt, Z. Phys. **C 67** (1995) 433.

[17] D.Yu. Bardin et al., Proceedings of the Workshop on HERA Physics, DESY 1996, ed. by G. Ingelman, A. De Roeck and R. Klanner, vol.1, 13, DESY 96-198, hep-ph/9609399.

[18] H1 BEMC Group, J. Bán et al., Nucl. Instr. and Meth. **A 372** (1996) 399.

[19] G. Altarelli and G. Martinelli, Phys. Lett. **B 76** (1978) 89.

[20] NMC Collaboration, M. Arneodo et al., Phys. Lett. **B 364** (1995) 107.

[21] E. Laenen et al., Nucl. Phys. **B 392** (1993) 162.

[22] A. Mueller, Nucl. Phys. **B 415** (1994) 373;
H. Navelet et al., Phys. Lett. **B385** (1996) 357.

[23] A. De Roeck and E.A. De Wolf, DESY preprint 96-143 (1996), hep-ph/9609203.
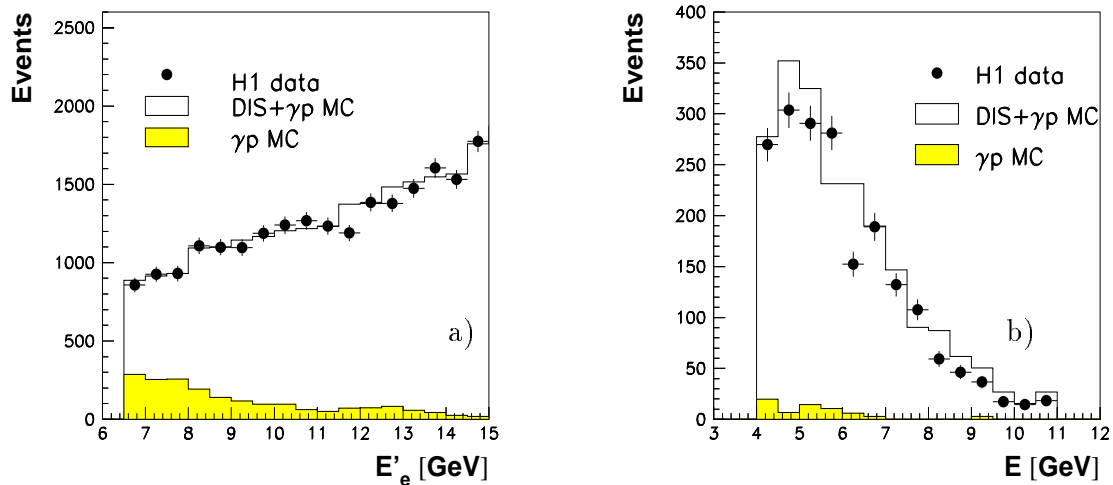
Figure 1: *Energy distributions of a) the highest energy and b) the next highest energy BEMC clusters for the final data sample. The simulated spectra are normalized to the luminosity of the data.*
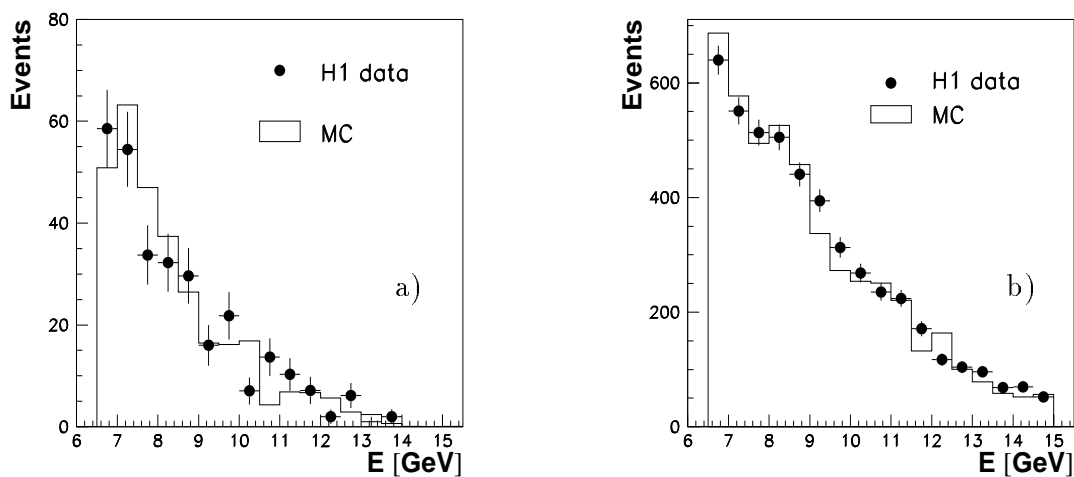

Figure 2: *Energy distributions of the highest energy cluster in the BEMC a) for photoproduction events in which the scattered positron was tagged and b) for the events rejected by the CIP requirement. The simulated spectra are normalized to the luminosity of the data.*
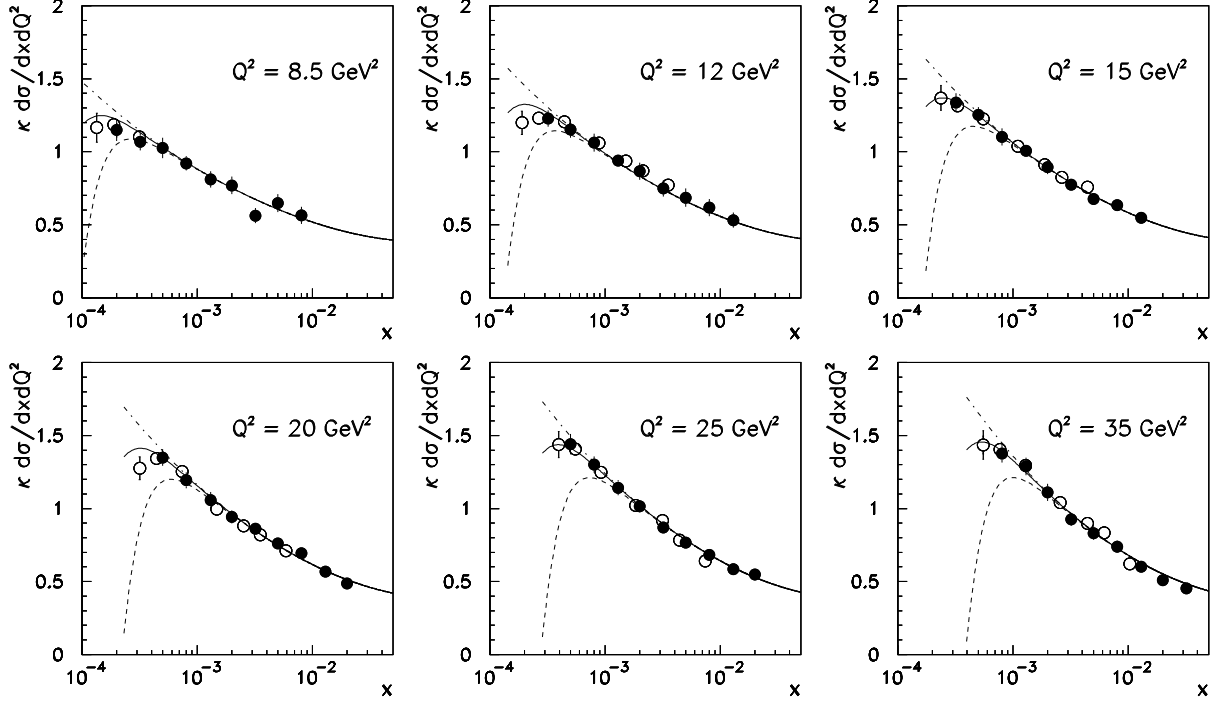
15

Figure 3: *Double differential cross section* $\kappa d\sigma/dxdQ^2 = F_2 - \frac{y^2}{Y_+}F_L$ *with* $\kappa = Q^4x/(2\pi\alpha^2 \cdot Y_+)$ *in six* Q^2 *bins as a function of* x. *For* $y > 0.6$ *this analysis (open points) extends the previously published measurement [6] (closed points) towards lower* x *and is drawn here with full errors. The open points at larger* x *are given without errors for ease of comparison with the data of [6]. The three lines represent calculated cross sections using for* F_2 *the QCD fit, as described in sect. 3.1, and three different assumptions for* F_L. *These are the two extremes,* $F_L = 0$ *(dashed-dotted line) and* $F_L = F_2$ *using* F_2 *from the QCD fit (dashed line), and* F_L *as calculated in NLO from the quark and gluon distributions determined by the QCD fit (solid line).*
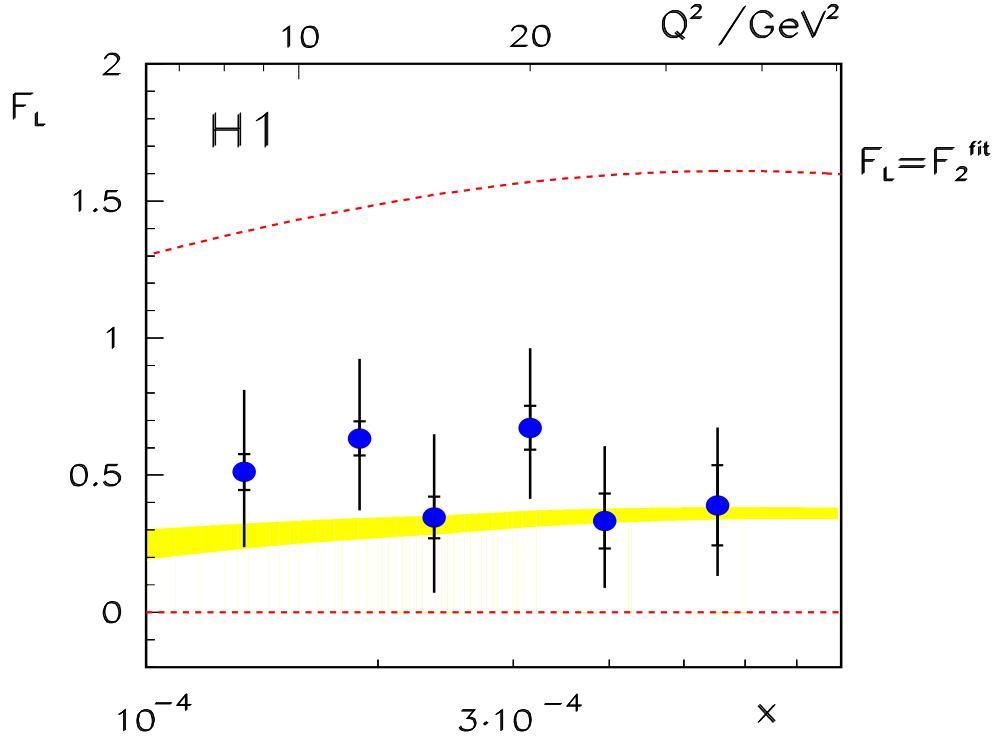
16

Figure 4: *Longitudinal structure function F_L as function of Q^2 or $x = Q^2/sy$ for $y = 0.7$. The inner error bars are the statistical errors. The full error bars represent the statistical and systematic errors added in quadrature. The error band represents the uncertainty of the calculation of F_L using the gluon and quark distributions, as determined from the NLO QCD analysis of the H1 data [6] for $y \leq 0.35$ and the BCDMS data [8]. The dashed lines define the allowed range of F_L values from $F_L = 0$ to $F_L = F_2$ where F_2 is given by the QCD fit.*